

the bulk and shear moduli (bands  $K_1$  and  $G$  in Fig. 3) of the lower mantle intersect at a potential temperature  $T \approx 1500$  K and  $\text{Si}/(\text{Mg} + \text{Fe}) \approx 0.78$ , a value between the values for pyrolite (8) and CI carbonaceous chondritic meteorites (22). Within the model uncertainties, pyrolitic and chondritic models are permissible, but pure enstatite (perovskite with no magnesiowüstite) models are not. For the higher values of  $\alpha$  and  $(\partial K/\partial T)_p$  that were determined in diamond-anvil experiments on  $(\text{Mg,Fe})\text{SiO}_3$  perovskite (9), there were no allowable (no intersection of the  $K_2$  and  $G$  bands) solutions in the compositional range between pure olivine and pure enstatite models and the potential temperature range between 600 and 2100 K. The uncertainty of 10% in the measured value of  $(\partial G/\partial T)_p$  results in variations of  $\pm 0.02$  in the  $\text{Si}/(\text{Mg} + \text{Fe})$  ratio and variations of  $\pm 100$  K in temperature. Adding Fe of 10 mole percent (mol%) to the perovskite phase in the model calculations (23) decreases  $G$  (by 8%), thus leading to lower potential temperatures and to compositions that are more olivine-rich.

References and Notes

1. T. S. Duffy and D. L. Anderson, *J. Geophys. Res.* **94**, 1895 (1989).
2. R. Jeanloz and E. Knittle, *Philos. Trans. R. Soc. London Ser. A* **328**, 377 (1989).
3. R. J. Hemley et al., in *High-Pressure Research: Application to Earth and Planetary Sciences*, Y. Syono and M. H. Manghnani, Eds. (American Geophysical Union, Washington, DC, 1992), pp. 183–189.
4. I. Jackson, *Geophys. J. Int.* **134**, 291 (1998).
5. Y. Wang and D. J. Weidner, *Pure Appl. Geophys.* **146**, 533 (1996).
6. A. Yeganeh-Haeri, *Phys. Earth Planet. Inter.* **87**, 111 (1994); A. Yeganeh-Haeri, D. J. Weidner, E. Ito, *Science* **243**, 787 (1989).
7. The values are  $\alpha \approx 2 \times 10^{-5}$  K and  $|(\partial K_p/\partial T)_p| \approx 2 \times 10^{-2}$  GPa/K [for example, (15); W. Utsumi et al., *Geophys. Res. Lett.* **22**, 1005 (1995); N. Funamori et al., *J. Geophys. Res.* **101**, 8257 (1996); G. Fiquet et al., *Phys. Earth Planet. Inter.* **105**, 21 (1998)].
8. The primitive mantle material called pyrolite was proposed by A. E. Ringwood [*Composition of the Earth's Mantle* (McGraw-Hill, New York, 1975), p. 295] to produce a typical basaltic magma on fractional melting. The initially proposed composition was one part of basalt and four parts of dunite.
9. The values are  $\alpha \approx 4 \times 10^{-5}$  K and  $|(\partial K/\partial T)_p| \approx 5 \times 10^{-2}$  GPa/K [for example, (2); E. Knittle et al., *Nature* **319**, 214 (1986); H. K. Mao et al., *J. Geophys. Res.* **96**, 8069 (1991); L. Stixrude, R. J. Hemley, Y. Fei, H. K. Mao, *Science* **257**, 1099 (1992)].
10. T. Gasparik, *J. Geophys. Res.* **95**, 15751 (1990).
11. From visual examination, perovskite specimens consisted of relatively large (up to 30  $\mu\text{m}$ ), transparent, colorless grains; finely polished surfaces revealed grain boundaries in equilibrium and an absence of twinning.
12. P. F. McMillan et al., in *Mineral Spectroscopy: A Tribute to Roger G. Burns*, M. D. Dyar, C. McCammon, M. W. Schaefer, Eds. (Geochemical Society, Washington, DC, 1996), pp. 175–190.
13. Recently, we have adapted ultrasonic interferometry techniques to a DIA-type, cubic anvil, high-pressure apparatus (SAM-85) installed on the superconducting wiggler beamline (X17B1) at the National Synchrotron Light Source of the Brookhaven National Laboratory [G. Chen, R. C. Liebermann, D. J. Weidner, *Science* **280**, 1913 (1998)].
14. In ultrasonic interferometry, a burst of high-frequency signal is applied to the piezoelectric transducer. The resultant elastic wave, propagating inside the

sample, produces a series of echoes. The travel time of an elastic wave through the sample is measured by observing constructive and destructive interferences among overlapped echoes as a function of carrier frequency.

15. Y. Wang et al., *Phys. Earth Planet. Inter.* **83**, 13 (1994).
16. The largest uncertainties in travel times ( $\pm 1\%$ ) originated from the anomalous travel-time dispersion. To minimize this dispersion, we chose a sufficiently large frequency window in our interference data, over which all collected travel times had a comparable dispersion shape. The travel times were averaged over a chosen frequency window to obtain  $G$  as a function of pressure and temperature. Discrepancies occurred for the data collected under initial compression at room temperature because of nonhydrostatic stresses. The deviation from hydrostatic conditions was accounted for by estimating pressures from subsets {200, 420} and {222, 220} of salt diffraction lines and by assigning the corresponding difference to a pressure uncertainty of the measurements.
17. J. Kung, thesis, Australian National University, Canberra (1997); J. Kung and S. M. Rigden, *Eos Trans. Am. Geophys. Union, Fall Meet. Suppl.* **78**, F803 (1997).
18. F. D. Stacey, *Phys. Earth Planet. Inter.* **89**, 219 (1995).
19. Y. Zhao and D. L. Anderson, *ibid.* **85**, 273 (1994).
20. Seismic tomography studies have shown that  $[(\partial \ln V_p)/(\partial \ln V_p)]_p \approx 2$  throughout the lower mantle [for example, A. Hales and H. Doyle, *Geophys. J. R. Astron. Soc.* **13**, 403 (1967); J. Woodhouse and A. Dziewonski, *Philos. Trans. R. Soc. London Ser. A* **328**,

- 291 (1989); X. Li et al., *Geophys. J. Int.* **105**, 649 (1991); G. Robertson and J. Woodhouse, *ibid.* **123**, 85 (1995)].
21. S. Karato, *Geophys. Res. Lett.* **20**, 1623 (1993).
22. W. F. McDonough and S.-s. Sun, *Chem. Geol.* **120**, 223 (1995).
23. The inclusion of Fe was assumed to reduce perovskite's  $G$  in a manner similar to the reduction of  $G$  in magnesiowüstite (5, 6).
24. We thank the personnel who contributed to the execution of these ultrasonic experiments in SAM-85 at the National Synchrotron Light Source (NSLS) of the Brookhaven National Laboratory: H. Kagi, J. Liu, H. Schay, K. Baldwin, P. Hoversen, B. Vitale, C. Koleda, and B. Huebsch. We especially thank Y. Fei and B. Mysen at the Geophysical Laboratory for helping with the Raman spectroscopy measurements; J. Hastings and D. Siddons at the NSLS for their technical support at the beamline X17B1, where this work was performed; J. Chen and D. Weidner for their support and encouragement in this new project; and Y. Wang for providing the pressure-volume-temperature data. These high-pressure experiments were conducted with the joint support of the State University of New York at Stony Brook and the NSF Science and Technology Center for High Pressure Research under Earth Sciences Division grant EAR 89-20239. This research was also supported by NSF grants to R.C.L. (EAR 93-04502 and 96-14612). This is Mineral Physics Institute contribution 226.

30 March 1998; accepted 16 June 1998

# Multi-Atom Resonant Photoemission: A Method for Determining Near-Neighbor Atomic Identities and Bonding

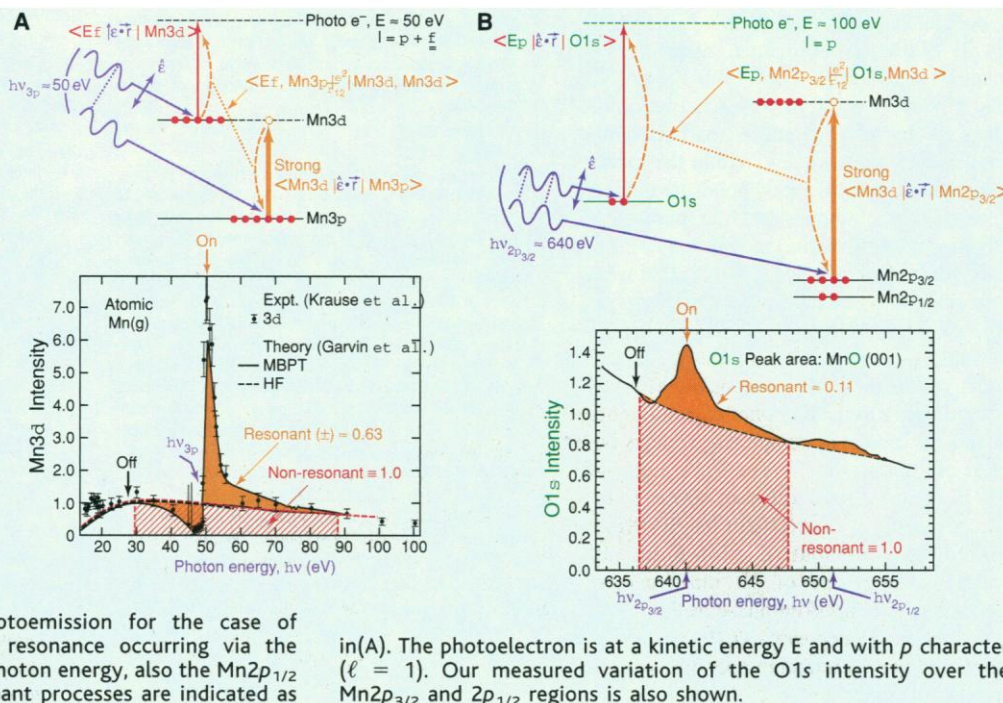
A. Kay, E. Arenholz, S. Mun, F. J. García de Abajo,\* C. S. Fadley,† R. Denecke,‡ Z. Hussain, M. A. Van Hove

Measurements and theoretical calculations are reported for an interatomic multi-atom resonant photoemission (MARPE) effect that permits direct determination of near-neighbor atomic identities (atomic numbers). MARPE occurs when the photon energy is tuned to a core-level absorption edge of an atom neighboring the emitting atom, with the emitting level having a lower binding energy than the resonant level. Large peak-intensity enhancements of 33 to 105 percent and energy-integrated effects of 11 to 29 percent were seen in three metal oxides. MARPE should also be sensitive to bond distance, bonding type, and magnetic order, and be observable via the secondary processes of x-ray fluorescence and Auger decay.

Several experimental techniques presently permit determining the bulk atomic structures of solids, including x-ray diffraction and extended x-ray absorption fine structure (EXAFS) (1). EXAFS is also element-specific via core-level electronic excitations and allows the local structure around each atomic type to be determined, specifically the radial positions of shells of neighboring atoms. If the atomic structure near solid surfaces is to be probed, then low energy electron diffraction (LEED) (2) and photoelectron diffraction (PD) (3) can be added to this list, with the latter also being element-specific via core excitation. Howev-

er, as powerful and widely used as the aforementioned methods are, none of them permits directly determining the type of atom that neighbors a given atom. That is, some of these techniques (such as EXAFS and PD) may be element-specific for the central atom in the structure, but there is no simple way to determine the near-neighbor atomic identities (atomic numbers) from them. Use can be made of the differences in electron-atom scattering strengths between different atoms in these last two methods, together with comparison of experiment with model calculations, but this is only unambiguous when

**Fig. 1. (A)** Single-atom resonant photoemission (SARPE) for the case of Mn3d emission from atomic Mn, with the resonance occurring via the Mn3p level. The direct excitation is indicated by the solid red arrow and the resonant process by a solid orange arrow (resonant excitation) and dashed orange arrows (autoionization decay). The key quantum-mechanical dipole and coulomb matrix elements involved are also indicated. The photoelectron is here predominantly  $f$  in character (angular momentum =  $\ell = 3$ ). The lower panel [from (5, 6)] also shows the measured variation of the Mn3d intensity with photon energy, together with two types of theoretical calculation: Hartree-Fock (HF) and many-body perturbation theory (MBPT). The solid orange and red cross-hatched areas represent the resonant and nonresonant contributions to intensity, respectively. **(B)** Multi-atom resonant photoemission for the case of O1s emission from MnO, with the resonance occurring via the Mn2p<sub>3/2</sub> level (or at a slightly higher photon energy, also the Mn2p<sub>1/2</sub> level). The direct excitation and resonant processes are indicated as



atomic numbers are relatively far apart, and is even then only semiquantitative.

We report an effect in soft x-ray absorption that should provide a direct probe of near-neighbor atomic number. This effect is related to the previously studied single-atom resonant photoemission (SARPE) (4–8), as illustrated in Fig. 1A. In this intra-atomic effect, the excitation of a photoelectron from one level in the atom (shown here as Mn3d from a gas-phase Mn atom) is enhanced by about a factor of 7 when the photon energy reaches 50 eV and is then just sufficient to excite a deeper-lying Mn3p electron in the same atom up to the first bound excited state (which will also be of Mn3d character). When this occurs, the very strong resonant Mn3p-to-Mn3d excitation can be considered to decay immediately so as to produce a free electron at the same energy as the photoelectron directly excited from Mn3d at the same photon energy, as shown by the dashed orange arrows in Fig. 1A. This resonant

decay process [often termed autoionization (4)] is simultaneous with and coherent with the usual direct excitation of the photoelectron. The variation of the intensity of the Mn3d photoelectrons has been measured by Krause *et al.* (5) as the photon energy passes over the Mn3p resonance region (see bottom of Fig. 1A); note the change in sign of the resonance effect as photon energy varies due to a change in phase between the direct and resonant channels, with the curve generally following what is termed a Fano profile (4). If the positive and negative effects of the resonance (solid orange areas) are integrated over the full energy range for which the resonance causes significant differences in intensity from a simple nonresonant Hartree-Fock (HF) theory (6), and are compared to the estimated nonresonant intensity (red cross-hatched areas), an overall effect of ~63% is found.

We have now asked whether such a process occurs as an interatomic effect between two neighboring atoms, for example, between O and Mn in a crystal of MnO (Fig. 1B). Such an effect we term multi-atom resonant photoemission (MARPE). We first considered the case of photoemission from the O1s level (a deep lying core electron with binding energy of ~530 eV) and asked whether this excitation can involve a resonance with the deeper lying Mn2p<sub>3/2</sub> and 2p<sub>1/2</sub> levels whose first excited 3d states occur at ~639 and 650 eV, respectively (9). The autoionization decay that would occur for the Mn2p<sub>3/2</sub> resonance (Fig. 1B; dashed orange arrows) involves the simultaneous de-excitation of Mn3d to Mn2p<sub>3/2</sub> and excitation of O1s to a free-electron state at the photoelectron ener-

gy. If such excitations exist and are strong enough to be measured relatively easily, we would expect them to provide a direct probe of near-neighbor atomic number. Implicit here is that all atoms have well-known and characteristic core-level binding energies (the minimum energies needed to release a photoelectron from a level) that can, in principle, be used as “fingerprints” of their presence through such resonances. Also, theoretical analysis (discussed below) indicates that the observation of MARPE in a given material implies a very close physical proximity of the emitting atom and the autoionizing atom.

We have searched for such effects in experiments at beamline 9.3.2 of the Advanced Light Source (ALS) in Berkeley, California (3, 10), which permits scanning photon energy continuously over the range from 30 to 900 eV. In our experimental geometry (Fig. 2A), the light was linearly polarized, with polarization vector  $\hat{e}$  lying in the plane of the figure. The higher brightness of the ALS (a third-generation synchrotron radiation source), coupled with the higher transmission and resolution of the rotatable Scienta ES200 electron spectrometer used to measure photoelectron spectra (3), permitted determination of photoelectron intensities rapidly enough to study any resonant effects as a function of the experimental parameters of photon energy  $h\nu$ , photoelectron emission direction ( $\theta, \phi$ ), and photon incidence angle ( $\theta_{h\nu}$ ), with  $\theta$  and  $\theta_{h\nu}$  being independently variable.

The samples we studied were low-index surfaces of single crystals of inorganic transition-metal compounds: MnO(001), Fe<sub>2</sub>O<sub>3</sub>(001), and La<sub>0.7</sub>Sr<sub>0.3</sub>MnO<sub>3</sub>(001), with the last one being of the so-called colossal magnetoresis-

A. Kay, S. Mun, C. S. Fadley, R. Denecke, Department of Physics, University of California at Davis, Davis, CA 95616, USA, and Materials Sciences Division, Lawrence Berkeley National Laboratory, Berkeley, CA 94720, USA. E. Arenholz, F. J. García de Abajo, M. A. Van Hove, Materials Sciences Division, Lawrence Berkeley National Laboratory, Berkeley, CA 94720, USA. Z. Hussain, Advanced Light Source, Lawrence Berkeley National Laboratory, Berkeley, CA 94720, USA.

\*Permanent address: Departamento de CCIA y Departamento de Física de Materiales, Universidad del País Vasco/EHU, 20080 San Sebastián, Spain.

†To whom correspondence should be addressed. E-mail: fadley@physics.ucdavis.edu

‡Present address: MAXLAB, Lund University, S-22100 Lund, Sweden.

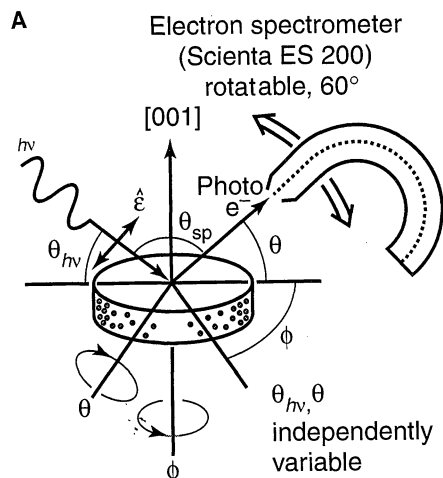
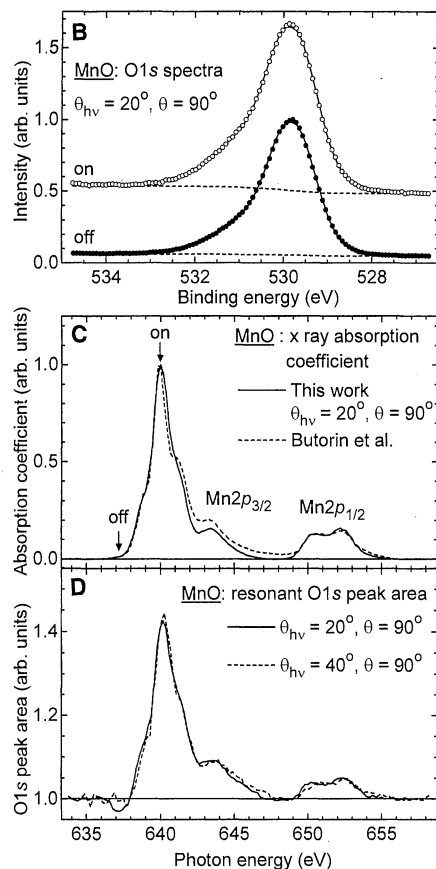


**Fig. 2.** (A) The experimental configuration, with various key elements and parameters defined. Berkeley's Advanced Light Source beamline 9.3.2 was used to provide photon energy ( $h\nu$ ) from 30 to 900 eV. All of the variables  $h\nu$ ,  $\theta_{h\nu}$ ,  $\theta_{sp}$ ,  $\theta$ , and  $\phi$  could be varied independently, subject only to  $\theta_{h\nu} + \theta_{sp} + \theta = 180^\circ$  [compare (3)]. (B) O1s photoelectron spectra for  $\theta_{h\nu} = 20^\circ$  and  $\theta = 90^\circ =$  normal emission: off-resonance at  $h\nu = 637.6$  eV (solid data points and lower curve) and on-resonance at  $h\nu = 640.2$  eV (open data points and upper curve). The inelastic background is shown as dashed curves. Note the increased background on-resonance. (C) X-ray absorption coefficient for MnO, as measured in this study from the energy dependence of the inelastic background under the O1s spectra (solid curve) and from (9) (data points). (D) O1s intensities (peak areas) above inelastic background for normal emission as a function of photon energy, with the smoothly varying nonresonant intensity at each energy (compare Fig. 1B) being subtracted and set to unity. Data are shown for  $\theta_{h\nu} = 20^\circ$  (solid curve) and  $40^\circ$  (dashed curve).

tive oxides with mixed  $Mn^{3+}$  and  $Mn^{4+}$  oxidation states. Oxygen is bound directly to Mn or Fe in all three of these materials, with nearest-neighbor bond distances of 2.23 Å, 1.96 to 2.09 Å, and 1.96 Å, respectively. The surfaces were prepared outside of vacuum and then cleaned by appropriate annealing in ultrahigh vacuum for MnO and  $Fe_2O_3$ , and including a high-temperature treatment with oxygen for  $Fe_2O_3$ . A high degree of surface crystalline order was verified in all three samples by O1s photoelectron diffraction measurements (3). In each case, we studied the resonance of O1s with the  $2p_{3/2}$  and  $2p_{1/2}$  levels of the transition-metal atom that is known to be bound directly to the oxygen, as shown schematically for the first case of MnO in Fig. 1B. In the perovskite-derived lattice of  $La_{0.7}Sr_{0.3}MnO_3$ , we have also studied resonances between O1s and  $La3d_{5/2,3/2}$  (distance of 2.52 Å) and between  $Mn2p$  and  $La3d_{5/2,3/2}$  (3.37 Å). For reference, the binding energies of the levels involved are: O1s = 532 eV;  $Mn2p_{3/2,1/2} = 644$  and 656 eV; and  $La3d_{5/2,3/2} = 837$  and 854 eV. Any level can, in principle, resonate with another level at higher binding energy, so possible pairs are: O1s with  $Mn2p$  (resonant photoelectron kinetic energy = K.E.  $\approx 110$  eV),



O1s with  $La3d$  (K.E.  $\approx 302$  eV), and  $Mn2p$  with  $La3d$  (K.E.  $\approx 184$  eV).

The  $Mn2p_{3/2}$  region yields the strongest peak in an x-ray absorption spectrum of MnO at approximately 640 eV (9), and thus is expected to give rise to the strongest interatomic resonance effects. Typical O1s spectra from MnO are shown off-resonance (solid points) and on-resonance (open points) in Fig. 2B. Note the much increased background intensity on-resonance due to inelastic scattering of electrons produced in the decay of the  $Mn2p_{3/2} \rightarrow 3d$  excitations through secondary Auger processes that are different from the resonant autoionization channel. We used the photon-energy dependence of this background intensity to measure the x-ray absorption coefficient of MnO in our experiment, and this is shown in Fig. 2C in direct comparison to an x-ray absorption spectrum measured previously by a different method (9). There is excellent agreement between the two curves. Spectra such as those in Fig. 2B have been analyzed by subtracting a background of general Shirley type (dashed curves in Fig. 2B) and simultaneously fitting each component with an analytical peak shape (Voigt

function) so as to derive accurate O1s peak intensities via peak areas. The curves in Fig. 2B are the results of such fits. Such photoelectron intensities were then determined as a function of photon energy. The final O1s intensity variations with energy for MnO are shown at the bottom of Fig. 1B for emission normal to the surface. An enhancement of intensity of  $\sim 43\%$  occurs at the peak of the  $Mn2p_{3/2}$  absorption, with smaller enhancements in the  $Mn2p_{1/2}$  region. These enhancements are relative to the monotonically varying underlying intensity that would be expected in the absence of any resonance (compare the atomic Mn data; bottom of Fig. 1A). The energy-integrated ratio of resonant to nonresonant intensities is  $\sim 11\%$ , or about one-fifth of that for the intraatomic case of Fig. 1A. These resonance intensity enhancements also follow very closely, although perhaps not identically, the x-ray absorption coefficient of Fig. 2C, as we show more clearly in Fig. 2D, in which a smooth polynomial has been subtracted from the data in Fig. 1B to allow for the nonresonant underlying intensity, and this new baseline set is equal to unity.

To confirm the physical origin of these effects, we also compared background-normalized resonance effects for two different x-ray incidence angles, but with the electron exit fixed along the normal (Fig. 2D). Because these two curves are essentially identical, we can conclude that these enhancement effects in MnO are due to MARPE and not to variations in the exciting x-ray flux near the surface resulting from the strong  $Mn2p$  absorption and attendant increases in the relative photoelectron intensities of different atoms because of their short electron escape depths in the 5 to 7 Å range (11, 12). This is because the effect does not change when  $\theta_{h\nu}$  changes and because the x-ray penetration depths are in any case still expected to be much larger than the electron escape depths at approximately 110 Å and 200 Å for  $\theta_{h\nu} = 20^\circ$  and  $40^\circ$ , respectively [as estimated from recent work on metallic Fe (13, 14) extrapolated to MnO]. The reflectivities of the x-rays at the  $Mn2p_{3/2}$  resonance are also estimated to be less than  $\sim 0.001$  and  $\sim 0.01$  at  $\theta_{h\nu} = 20^\circ$  and  $40^\circ$ , respectively (14, 15), thus indicating that the electric field strength near the surface cannot change significantly because of the onset of significant reflection. Finally, the electron escape depths cannot change from off-resonance to on-resonance, since the overall electronic structure and electronic states for inelastic scattering are not significantly perturbed by our flux of x-rays (12).

Resonance enhancements were also seen in the other two oxide samples. Our measured x-ray absorption coefficient for  $Fe_2O_3$  is shown in Fig. 3A, where it is compared to a

prior measurement with higher resolution by Kuiper *et al.* (16), again showing excellent agreement. In Fig. 3B, the resonant O1s peak area as measured over the  $\text{Fe}2p_{3/2,1/2}$  region and for photoelectron emission normal to the  $\text{Fe}_2\text{O}_3(001)$  surface is shown as the solid curve, with the smoothly varying nonresonant intensity underlying it used for normalization. The resonance exhibits a maximum 62% peak intensity enhancement and an energy-integrated effect over the  $2p_{3/2}$  region of 705 to 720 eV of 24%. The enhancement again follows very closely the x-ray absorption curve, but is not identical to it. Also in Fig. 3B, we show the normalized resonant intensity for an electron takeoff angle of  $45^\circ$  as the dashed curve. This curve is again similar to the x-ray absorption coefficient and perhaps closer to it than for normal emission; here, the energy-integrated effect is 17%. A significant difference between the curves for the two emission directions indicates an angular dependence in MARPE. For  $\text{La}_{0.7}\text{Sr}_{0.3}\text{MnO}_3(001)$ , we show the x-ray absorption coefficient over the  $\text{Mn}2p_{3/2,1/2}$  re-

gion in Fig. 3C, including both our measurement (solid curve) and that from a prior study [dashed curve from (17)], and the normalized O1s intensity in resonance with it in Fig. 3D. There is a resonant peak increase at the  $2p_{3/2}$  position of about 33%, and a concomitant energy-integrated effect of 17%. The resonance is again seen to follow very closely the  $\text{Mn}2p$  absorption curve for this material (17). Although not shown here, the O1s intensity is also found to resonate with the  $\text{La}3d_{5/2,3/2}$  levels, with very large peak enhancements of up to 92 to 105% and an energy-integrated effect over  $\text{La}3d_{5/2}$  of 29%. Finally, Fig. 3E shows an analogous normalized resonant enhancement of the  $\text{Mn}2p$  intensity with the  $\text{La}3d_{5/2}$  and  $3d_{3/2}$  levels; this resonance in turn follows closely what we measured for the  $\text{La}3d$  x-ray absorption coefficient, and it is also in good agreement with prior x-ray absorption data for La metal (18). Although the surface of this last epitaxially-grown sample was in no way treated after insertion into ultrahigh vacuum, we nonetheless were able to detect all three possible resonance effects:

O with Mn and La, and Mn with La.

We also carried out theoretical calculations for the O1s-Mn $2p_{3/2}$  resonance in  $\text{MnO}(001)$  (19), based on an extension of the model used previously to describe intra-atomic effects (7). The relevant interactions and quantum-mechanical matrix elements involved are indicated in Fig. 1. Specializing to the MARPE case, we have the usual dipole excitation by light with polarization vector  $\hat{\epsilon}$  of an O1s electron to a  $p$  photoelectron at kinetic energy  $E$  ( $\langle E_p | \hat{\epsilon} \cdot \vec{r} | O1s \rangle$ ) and of a  $\text{Mn}2p_{3/2}$  electron to the first unoccupied  $\text{Mn}3d$  level ( $\langle \text{Mn}3d | \hat{\epsilon} \cdot \vec{r} | \text{Mn}2p_{3/2} \rangle$ ), and the auto-ionization of the  $\text{Mn}3d$  state via a coulomb interaction coupling the Mn and O electrons ( $\langle E_p, \text{Mn}2p_{3/2} | e^2/r_{12} | O1s, \text{Mn}3d \rangle$ ). A non-zero coulomb interaction of this type only requires wave function overlap on either atomic center (that is,  $E_p$  with O1s and  $\text{Mn}2p_{3/2}$  with  $\text{Mn}3d$ ), but not between centers. The final formula for O1s intensity can then be written as an absolute value squared of the sum of the usual dipole excitation and resonance products like  $\langle E_p, \text{Mn}2p_{3/2} | e^2/r_{12} | O1s, \text{Mn}3d \rangle \langle \text{Mn}3d | \hat{\epsilon} \cdot \vec{r} | \text{Mn}2p_{3/2} \rangle$ . The resonance terms must also be summed over all Mn atoms surrounding a given O emitter; hence, the "multi-atom" nomenclature. The photoelectron wave function  $\langle E_p |$  has also been calculated using a new multiple scattering cluster formalism so as to allow for all diffraction effects (20). Numerical values for the relevant integrals needed have been calculated directly using atomic wave functions and checked in certain cases against previously published values (7). More detailed expressions and discussion of our theoretical modeling appear elsewhere (19, 20).

These calculations indicate that the overall resonance enhancement as energy-integrated over  $\text{Mn}2p_{3/2}$ -derived absorption features should be  $\sim 2.5\%$ . Although this value is much less than the  $\sim 43\%$  peak enhancement seen in Fig. 2D, comparing these two numbers is not correct, because we cannot adequately predict the distribution of this resonant intensity in energy without a better description of the energies and lifetimes of the various intermediate many-electron states (19), as done previously in the theory of SARPE (7). Thus, it is more accurate to compare this theoretical number with the enhancement as integrated over the full range of intensity involved with  $\text{Mn}2p_{3/2}$  excitation, which yields about 11%, as noted previously. Our theoretical prediction is thus about four times smaller than the experimental value, but given the approximations made, this level of disagreement is not surprising. Based on prior experience with the theory of SARPE (7), additional factors beyond our model which would be expected to increase the theoretical value are (i) inclusion of covalent

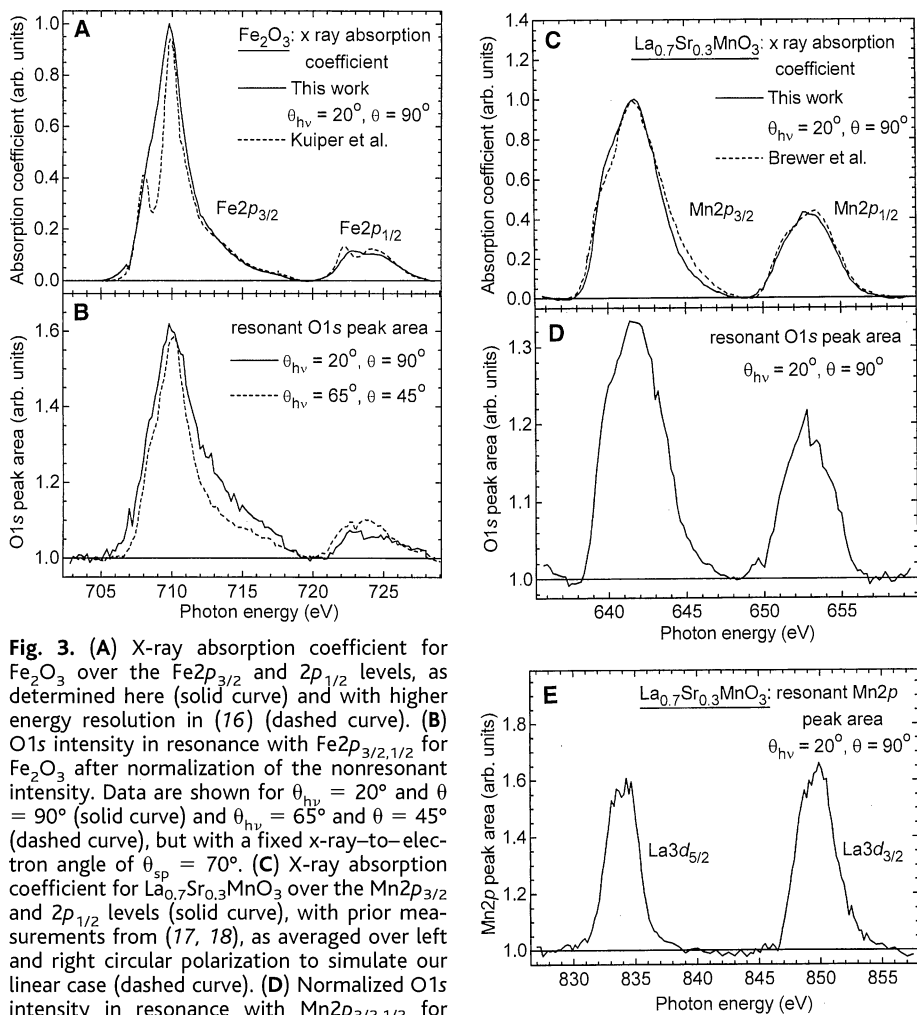


**Fig. 3.** (A) X-ray absorption coefficient for  $\text{Fe}_2\text{O}_3$  over the  $\text{Fe}2p_{3/2}$  and  $2p_{1/2}$  levels, as determined here (solid curve) and with higher energy resolution in (16) (dashed curve). (B) O1s intensity in resonance with  $\text{Fe}2p_{3/2,1/2}$  for  $\text{Fe}_2\text{O}_3$  after normalization of the nonresonant intensity. Data are shown for  $\theta_{\text{hv}} = 20^\circ$  and  $\theta = 90^\circ$  (solid curve) and  $\theta_{\text{hv}} = 65^\circ$  and  $\theta = 45^\circ$  (dashed curve), but with a fixed x-ray-to-electron angle of  $\theta_{\text{sp}} = 70^\circ$ . (C) X-ray absorption coefficient for  $\text{La}_{0.7}\text{Sr}_{0.3}\text{MnO}_3$  over the  $\text{Mn}2p_{3/2}$  and  $2p_{1/2}$  levels (solid curve), with prior measurements from (17, 18), as averaged over left and right circular polarization to simulate our linear case (dashed curve). (D) Normalized O1s intensity in resonance with  $\text{Mn}2p_{3/2,1/2}$  for  $\text{La}_{0.7}\text{Sr}_{0.3}\text{MnO}_3$  ( $\theta_{\text{hv}} = 20^\circ$  and  $\theta = 90^\circ$ ). (E) Normalized  $\text{Mn}2p$  intensity in resonance with  $\text{La}3d_{5/2,3/2}$  for  $\text{La}_{0.7}\text{Sr}_{0.3}\text{MnO}_3$  ( $\theta_{\text{hv}} = 20^\circ$  and  $\theta = 90^\circ$ ).

bonding effects, (ii) the polarization of electrons around both the  $Mn2p_{3/2}$  and  $O1s$  holes involved, and (iii) a more realistic treatment of the many-electron wave functions involved in the dipole and coulomb matrix elements, including configuration interaction effects. Theory also predicts a variation of the resonance effects with photoelectron emission angle due to photoelectron diffraction effects that is at least qualitatively seen in our data for the azimuthal angle ( $\phi$ ) dependence of intensities on and off the  $Mn2p_{3/2}$  resonance (21). Finally, our theoretical analysis suggests that these effects will die off approximately as  $1/(\text{distance-to-neighbor})^3$ . Thus, MARPE should be primarily sensitive to the nearest neighbors of a certain type of atom, and the observation of it should permit directly determining the atomic number of these nearest neighbors. Some next-nearest-neighbor sensitivity is also evident, as seen in our data for  $La_{0.7}Sr_{0.3}MnO_3$  between Mn and La (see Fig. 3E).

Several future directions of exploration and application of this effect can be pointed out. MARPE intensity enhancements are expected to be very sensitive to small changes in bond distances, bonding type, or both; for example, it may be possible to study the changes in the Mn-O distance thought to occur in the colossal magnetoresistive materials due to Jahn-Teller distortions (22). The well-known chemical shifts in photoelectron kinetic energies (3) should also permit measurement of resonances separately around different chemically distinct species. Although we used single crystals to better define the present data, there is no general requirement of a single-crystal specimen, thus broadening applicability considerably. MARPE effects should also be observable in free molecules, probably with reduced intensity if the number of near neighbors of a given type is lower, but perhaps with enhanced intensity if the resonant excited level is a more delocalized molecular orbital which better couples the several atoms involved. Here, we used photoelectrons emitted from the near-surface region to detect these resonances, but they should also be present in secondary fluorescent soft x-rays or Auger electrons resulting from the filling of the primary hole on the emitter. With x-ray detection, the experiment would become more bulk sensitive, considerably widening its applicability to include perhaps systems of biological interest, although a careful allowance for the enhanced absorption of the exciting flux at resonance would be needed to unambiguously detect the resonant enhancement. Atoms at buried interfaces should also be directly detectable via MARPE between a constituent of one side of the interface and a constituent of the other side. Finally, exciting with circularly polarized radiation on magnetic samples should lead to resonant photoelectron spin polarization or

magnetic dichroism effects, or both, in these resonances, yielding a probe of near-neighbor magnetic order.

References and Notes

1. E. A. Stern, M. Newville, B. Ravel, Y. Yacoby, D. Haskel, *Physica B* **208-209**, 117 (1995); M. Newville et al., *ibid.*, p. 154; and references therein.
2. M. A. Van Hove, W. H. Weinberg, C.-M. Chan, *Low Energy Electron Diffraction* (Springer-Verlag, Heidelberg, Germany, 1986).
3. C. S. Fadley et al., *Prog. Surf. Sci.* **54**, 341 (1997), and references therein.
4. U. Fano and J. W. Cooper, *Rev. Mod. Phys.* **40**, 493 (1968).
5. M. O. Krause, T. A. Carlson, A. Fahlman, *Phys. Rev. A* **30**, 1316 (1984), and references therein.
6. L. J. Garvin, E. R. Brown, S. L. Carter, H. P. Kelly, *J. Phys. B* **16**, L269 (1983).
7. A. Tanaka and T. Jo, *J. Phys. Soc. Jpn.* **63**, 2788 (1994), and references therein.
8. M. Weinelt et al., *Phys. Rev. Lett.* **78**, 967 (1997), and references therein.
9. S. M. Butorin, J.-H. Guo, M. Magnuson, P. Kuiper, J. Nordgren, *Phys. Rev. B* **54**, 4405 (1996).
10. Z. Hussain et al., *J. Electron Spectrosc. Relat. Phenom.* **80**, 401 (1996).
11. C. J. Powell, A. Jablonski, S. Tanuma, D. R. Penn, *ibid.* **68**, 605 (1994).
12. C. J. Powell, personal communication.
13. J. Stohr and R. Nakajima, *IBM J. Res. Dev.* **42**, 73 (1998).

14. J. Kortright, unpublished results for Fe.
15. E. Gullikson, Center for X-ray Optics, Lawrence Berkeley National Laboratory, public access program for calculating x-ray penetration depths and reflectivities available at [www-cxro.lbl.gov](http://www-cxro.lbl.gov)
16. P. Kuiper, B. G. Searle, P. Rudolf, L. H. Tjeng, C. T. Chen, *Phys. Rev. Lett.* **70**, 1549 (1993).
17. M. A. Brewer et al., *Advanced Light Source Compendium of User Abstracts and Technical Reports*, Report LBNL-39981, UC-411 (Lawrence Berkeley National Laboratory, Berkeley, CA, 1997), p. 411; K. Krishnan, personal communication.
18. B. T. Thole et al., *Phys. Rev. B* **32**, 5107 (1985).
19. A fuller treatment of MARPE theory is available as supplementary material via the *Science* Web site at [www.sciencemag.org/feature/data/981789.shl](http://www.sciencemag.org/feature/data/981789.shl)
20. F. J. García de Abajo, in preparation.
21. A. Kay, E. Arenholz, S. Mun, C. S. Fadley, data not shown.
22. S. J. L. Billinge, R. G. DiFrancesco, G. H. Kwei, J. J. Neumeier, J. D. Thompson, *Phys. Rev. Lett.* **77**, 715 (1996).
23. We are indebted to M. P. Klein and J. Kortright for helpful discussions, and to S. A. Chambers and K. Krishnan for providing samples. Supported by the Office of Energy Research, Materials Sciences Division, of the U.S. Department of Energy, under contract DE-AC03-76SF00098. Additional support from the Miller Institute (E.A.), the D.F.G.-Germany (R.D.), and the Basque Government (F.J.G.deA.) is also gratefully acknowledged.

6 April 1998; accepted 9 June 1998

## Visualization of Three-Dimensional Chaos

G. O. Fountain, D. V. Khakhar,\* J. M. Ottino†

Most chaotic mixing experiments have been restricted to two-dimensional, time-periodic flows, and this has shaped advances in theory as well. A prototypical, bounded, three-dimensional flow with a moderate Reynolds number is presented; this system lends itself to detailed experimental observation and allows for high-precision computational inspection. The flow structure, captured by means of cuts with a laser sheet (experimental Poincaré section), was visualized with the use of continuously injected fluorescent dye streams and revealed detailed chaotic structures with high-period islands.

Mixing is important in industry and ubiquitous in nature. Mixing-related problems may account for from 0.5 to 3% of the \$750 billion per year output value of U.S. chemical industries (1). In nature, examples of mixing include mantle convection (2, 3) and dispersion in oceans (4, 5) and in the atmosphere (6, 7). Over the last 10 years, there have been significant advances in our understanding of mixing (8, 9), which can be traced back to a clear connection between mixing and chaos as well as to careful experiments in prototyp-

ical flows (10). However, with few exceptions (11, 12), experiments have been restricted to two-dimensional (2D) time-periodic flows, and consequently this has shaped theoretical advances as well.

Studies with idealized 2D flows have helped visualize chaos and have been instrumental for many applications. In two dimensions passive dye structures in time-periodic flows evolve in an iterative fashion: an entire structure is mapped into a new structure that has persistent large-scale features but also finer and finer scale features that are revealed at each period of the flow. Unmixed regions (regular islands) translate, stretch, and contract periodically; they represent the primary obstacle to efficient mixing. Particle trajectories in chaotic regions separate exponentially fast, and material filaments are continuously stretched and folded by means of horseshoes (10). Formally, the advection equations are a

Laboratory for Fluid Mechanics, Chaos, and Mixing, Department of Chemical Engineering, McCormick School of Engineering and Science, Northwestern University, Evanston, IL 60208-3120, USA.

\*Permanent address: Department of Chemical Engineering, Indian Institute of Technology-Bombay, Powai, Bombay 400076, India.

†To whom correspondence should be addressed. E-mail: [ottino@chem-eng.nwu.edu](mailto:ottino@chem-eng.nwu.edu)